MRI SATURATION AND TRANSITION TO TURBULENCE

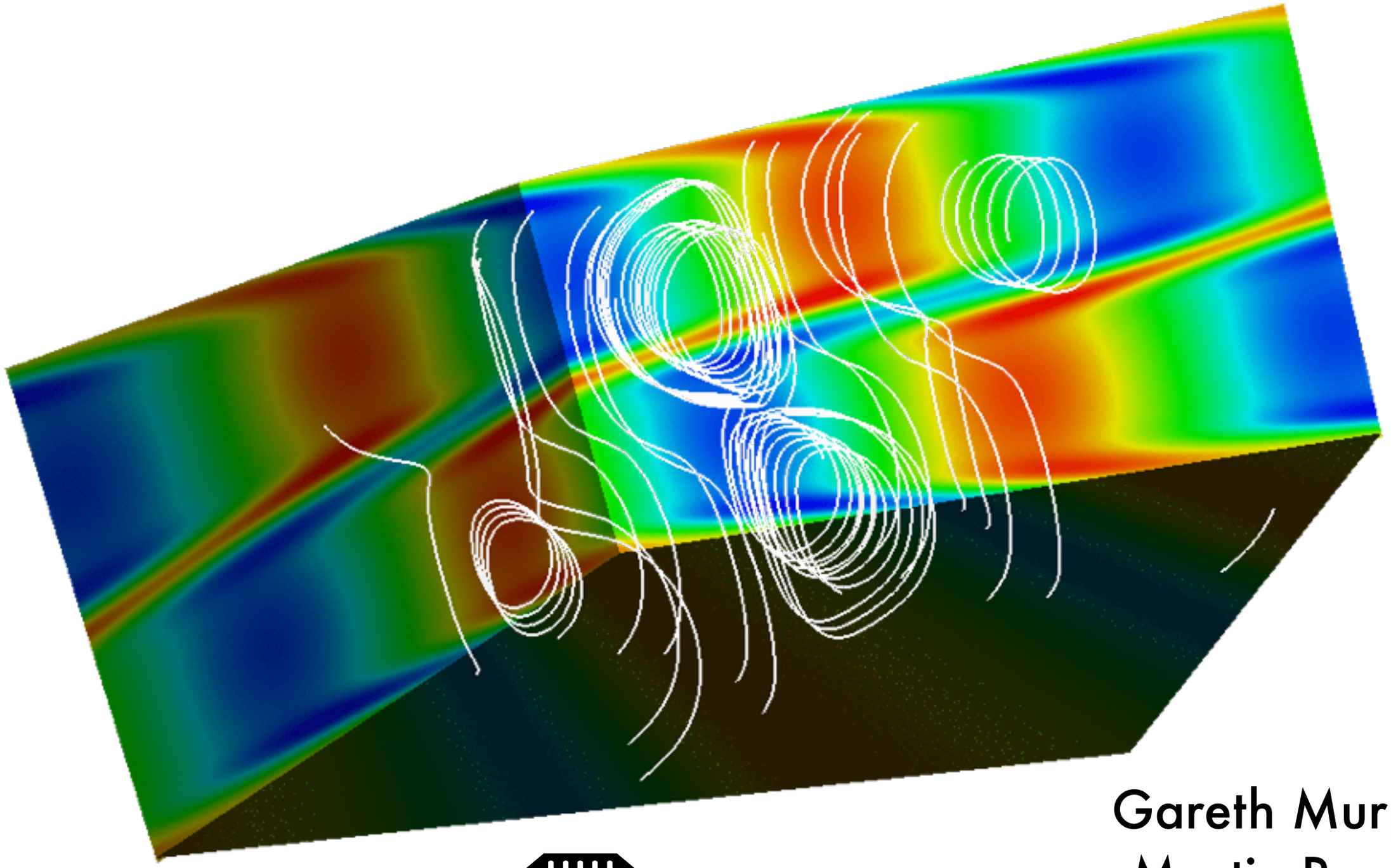

Gareth Murphy
Martin Pessah

The Niels Bohr
International Academy

How does the MRI saturate?

- Parasite modes? (Goodman & Xu (1994); Pessah & Goodman (2009); Latter et al. (2009); Pessah (2010) Longaretti & Lesur (2010), this talk)

- Flattening of the background shear profile? (Knobloch & Julien (2005))

- Saturation via diversion of energy into generating magnetosonic waves, or generation of large-scale magnetic fields via a dynamo process? (Liverts et al. (2012), Vishniac (2011) Brandenburg (1995))

MRI Exact Solutions

- MRI exact nonlinear modes exist but are unstable to Kelvin-Helmholtz and tearing mode instabilities (Goodman & Xu 1994, Pessah 2010)

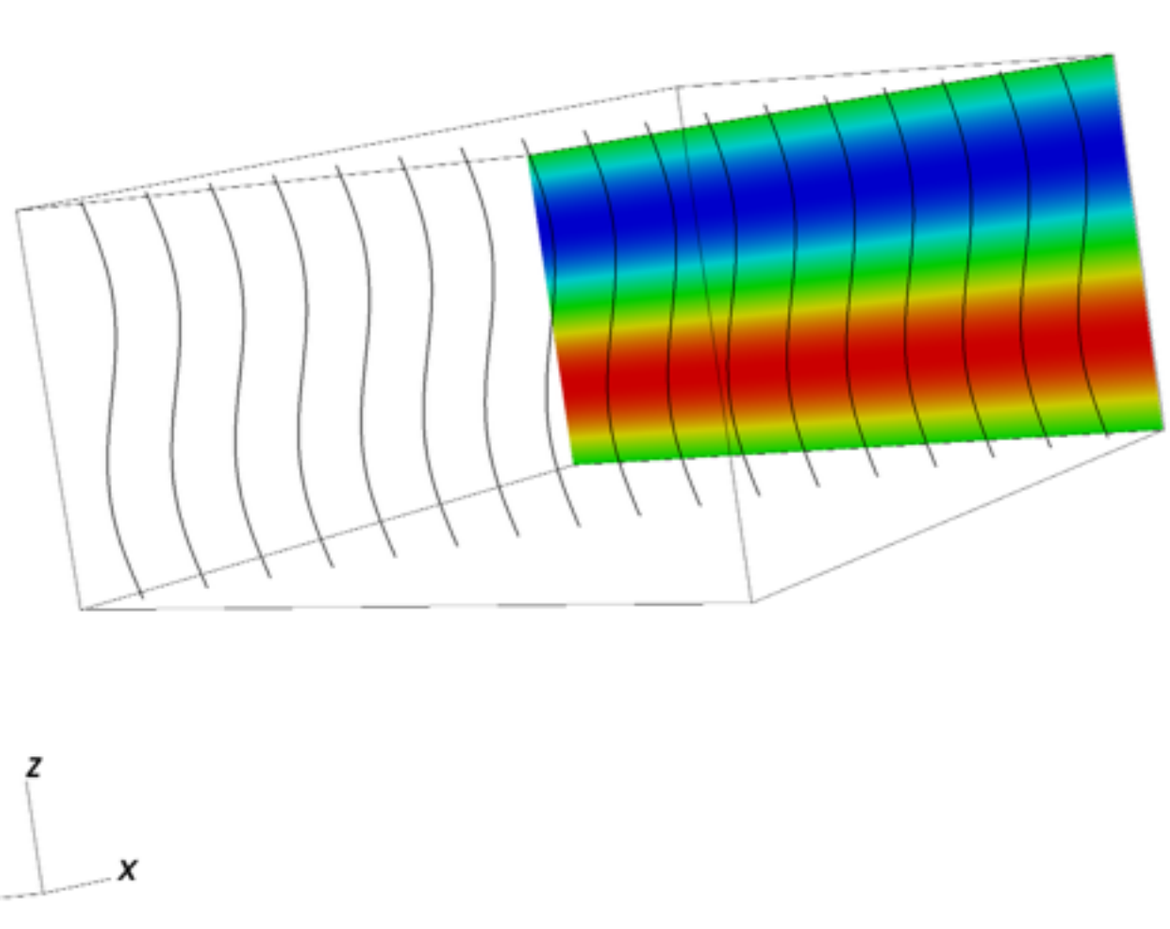

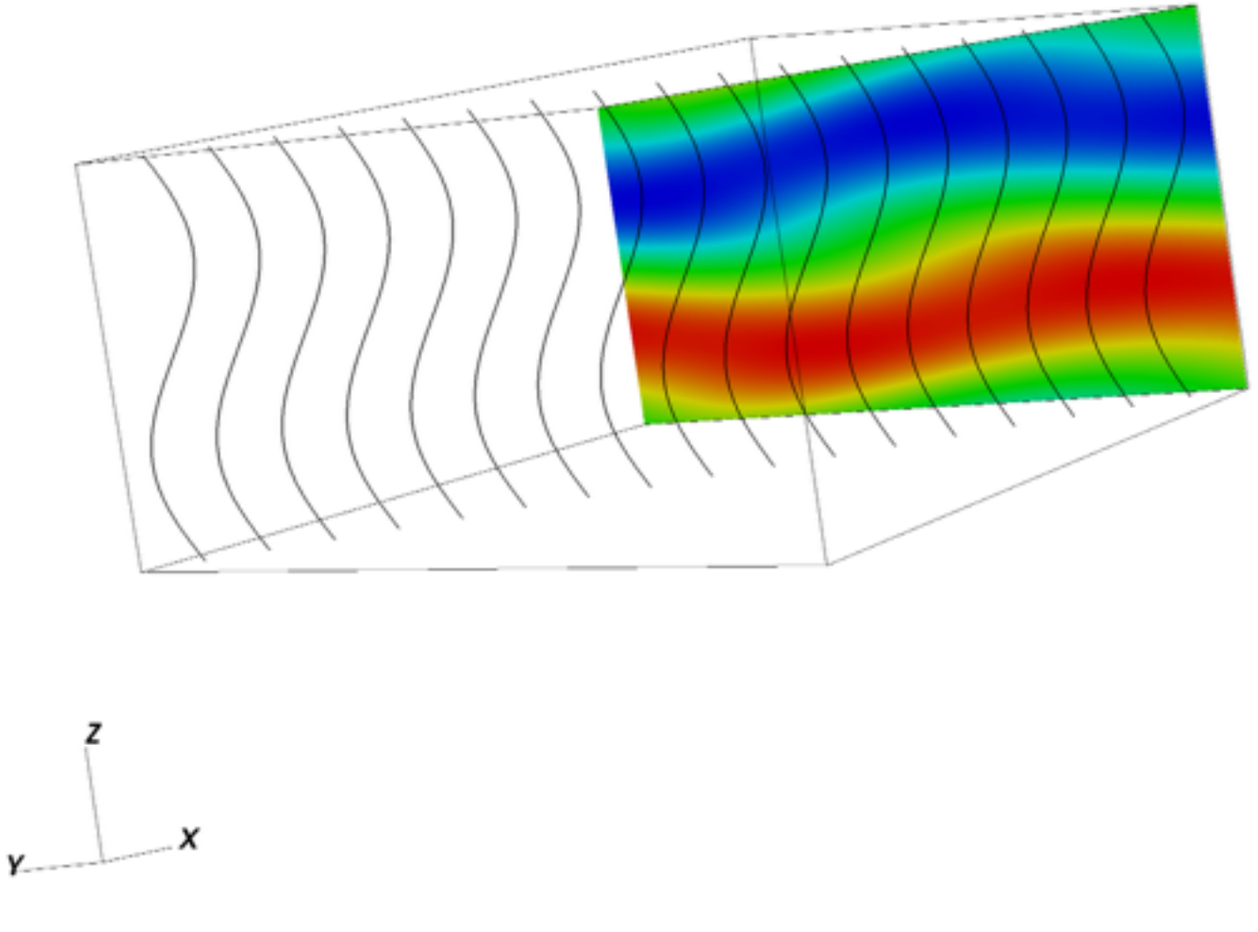

KH parasite mode

analytical

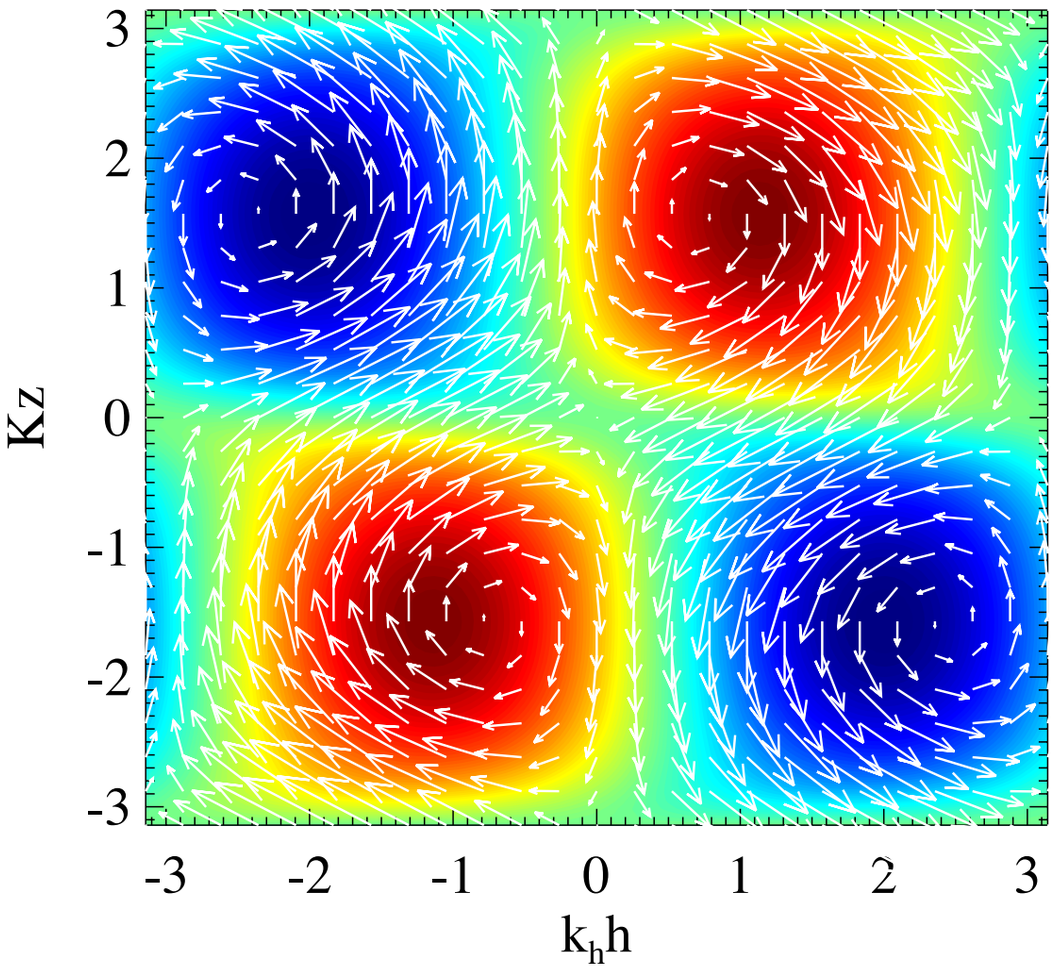

- Analytical prediction (Goodman & Xu, 1994) - 2d structure from Pessah (2010)
- Background has been subtracted
- Colourmap= vorticity, arrows=velocity field

numerical

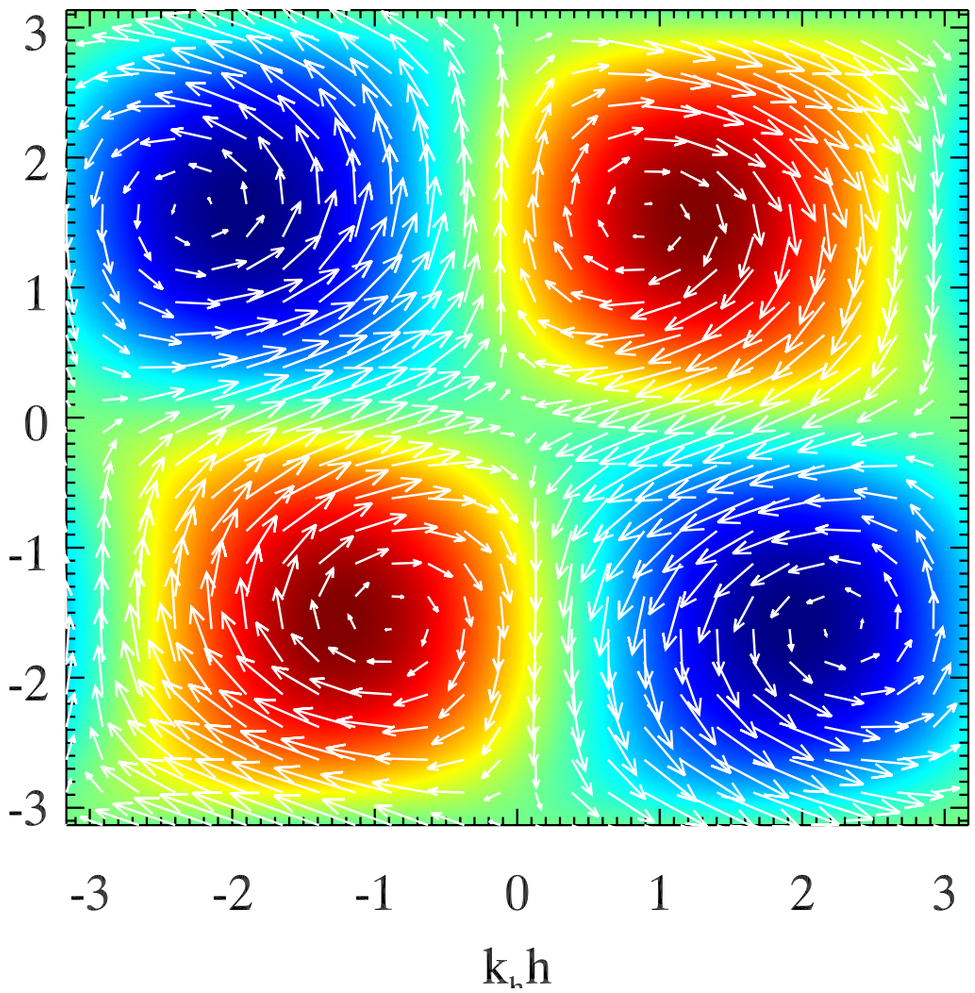

- 2D HD simulations
- Reproduces predicted vorticity and velocity
- Typical alternating polarity cellular vortices

Simplified model

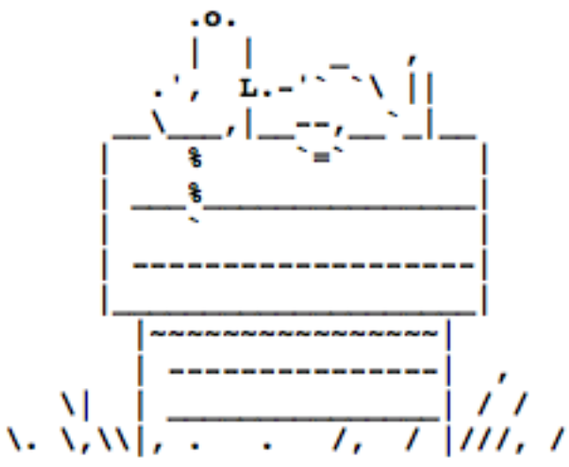

- Unstratified shearing box
- SNOOPY code (G. Lesur)
- Ideal MHD, isothermal, constrained transport

$$L = \sqrt{\frac{16}{15}} 2\pi \frac{v_a}{\Omega_0}$$

- Vertical magnetic field
- Box aspect ratio 2L:2L:1L
- L=wavelength of fastest growing mode
- single fastest-growing MRI mode perturbed t=0
- Mode perturbed t=6 orbits

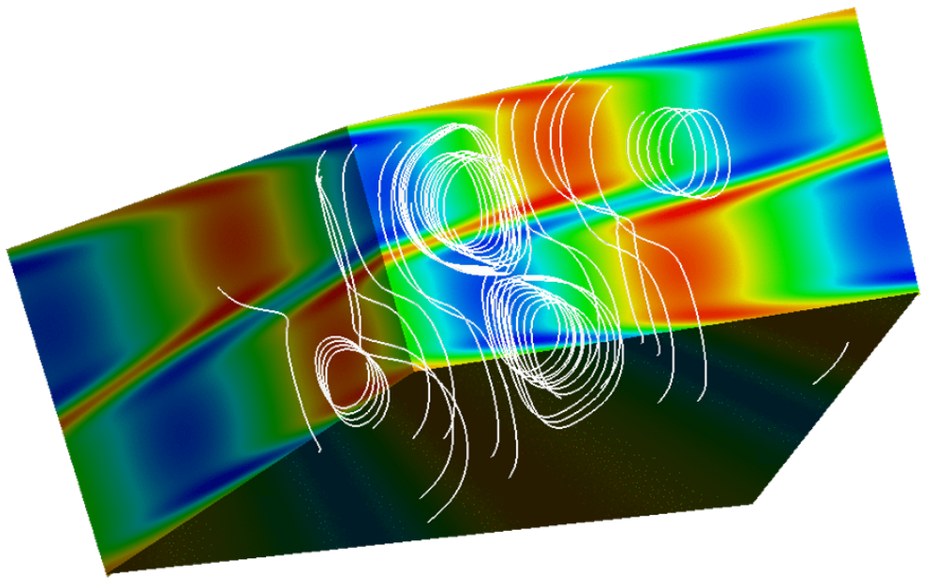

MRI growing @ exp(0.75t)

parasite growing @ exp(exp(0.75t))

$v_{x,y,z}$, $B_{x,y,z}$

10.0000
1.0000
0.1000
0.0100
0.0010
0.0001

v_x
v_y
v_z
b_x
b_y
b_z
exp(0.75t)

0 1 2 3 4 5 6

time (orbits)

10^{0}

10^{-2}

10^{-4}

10^{-6}

$v_{x,y,z}$, $B_{x,y,z}$

6.0 6.1 6.2 6.3 6.4 6.5

time (orbits)

v_x
v_y
v_z
B_x
B_y
B_z
exp(0.75t)

KH: decaying vs MRI-driven

Decaying KH

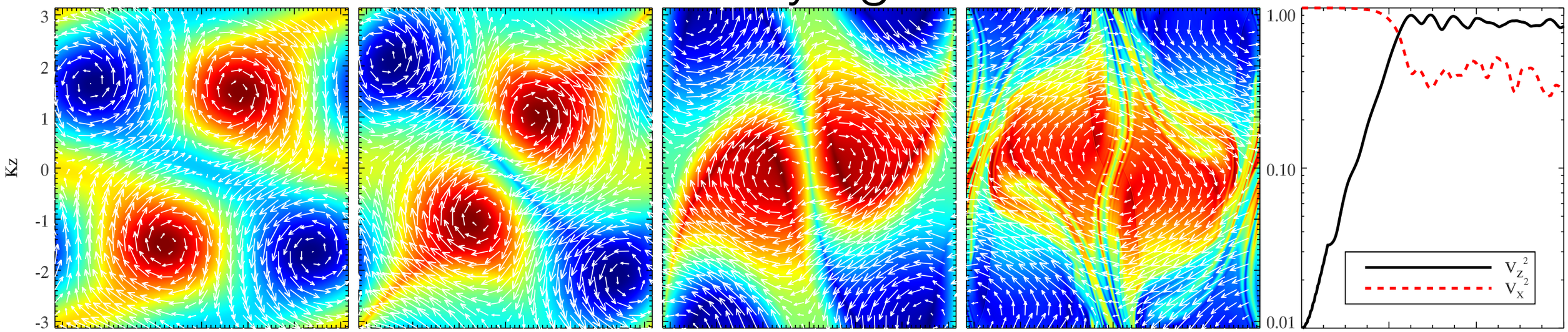

MRI-driven KH

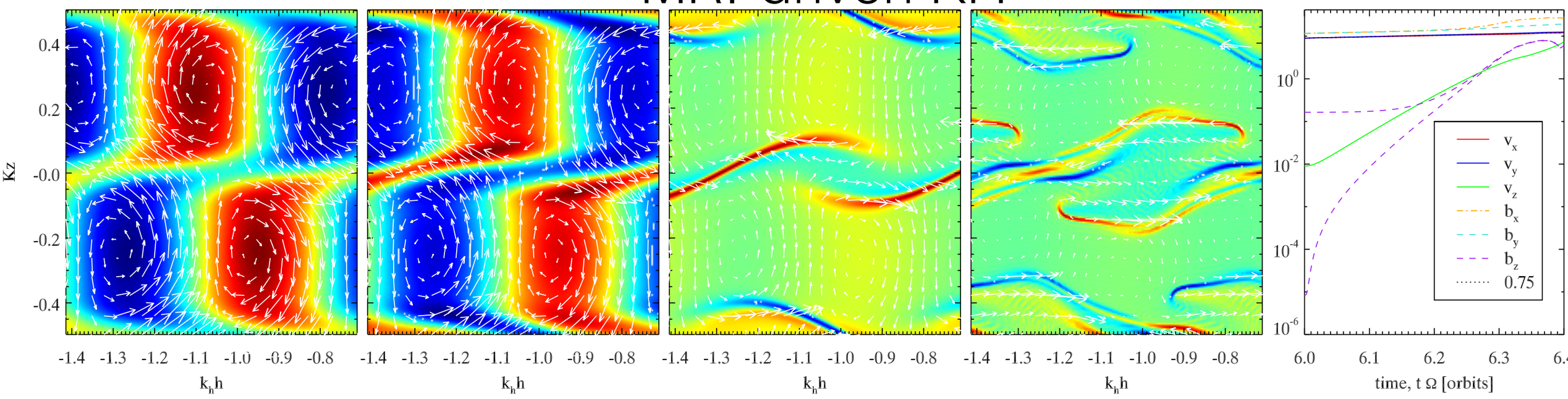

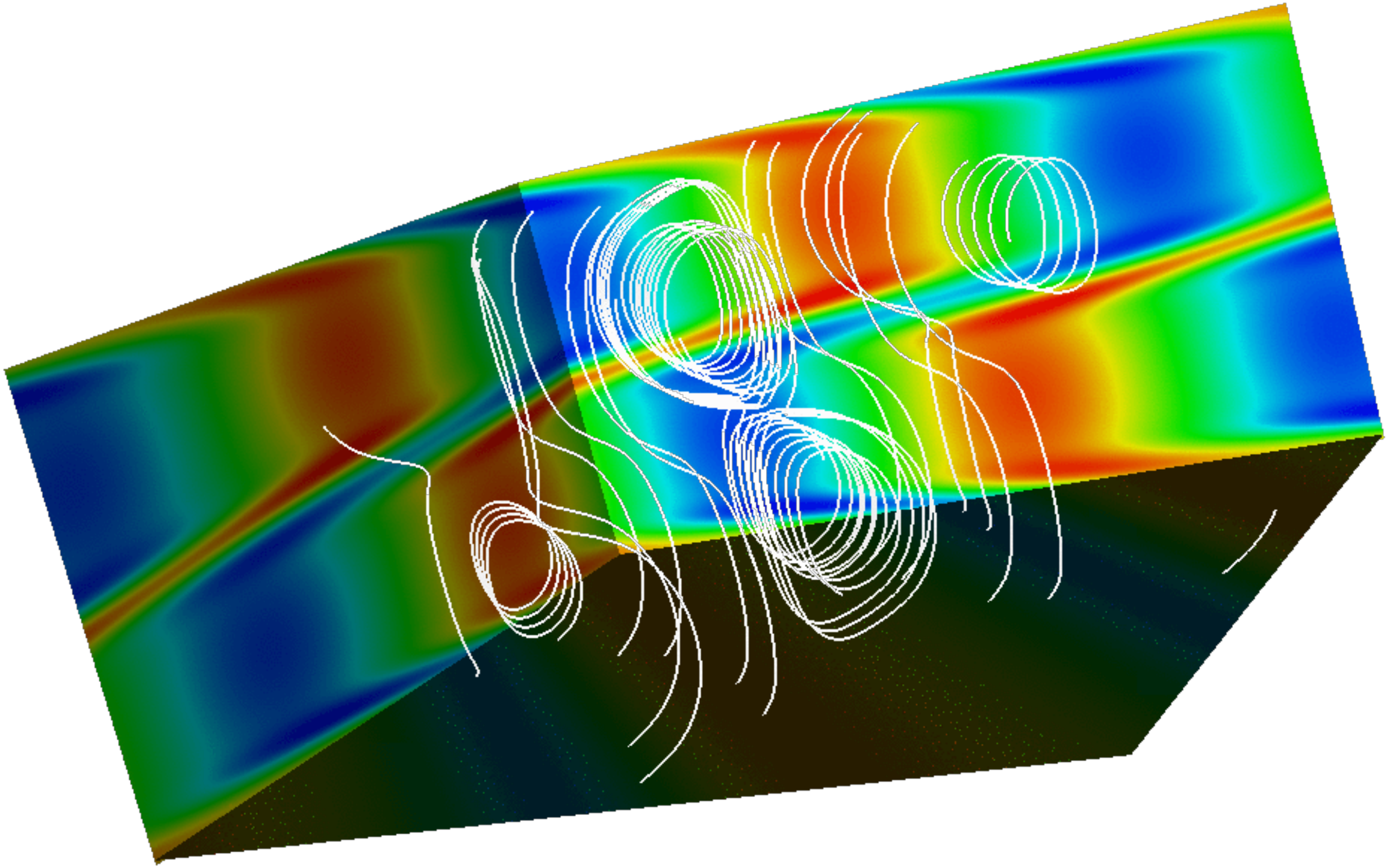

Anisotropy

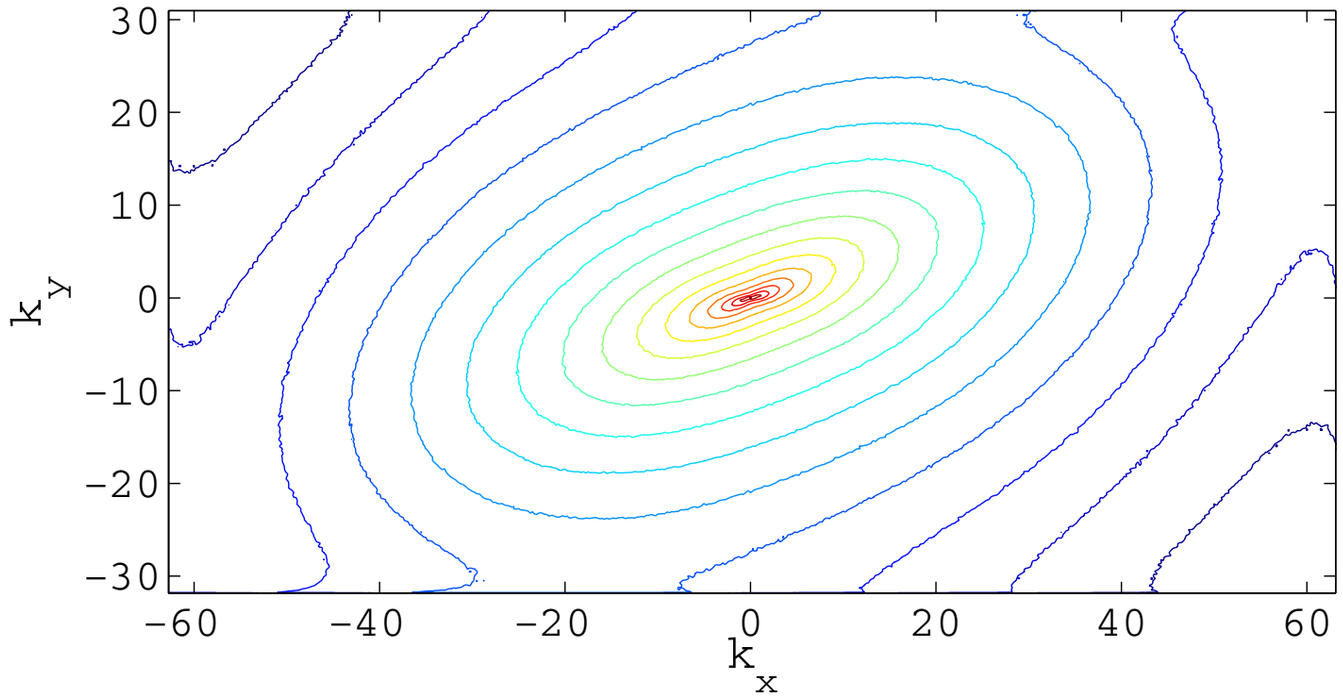

DFT of magnetic energy averaged in kz (Lesur & Longaretti 2011)

- In late linear regime, $B_x = B_y > B_z$
- In the turbulent regime, $B_y > B_x, B_z$
- => flow anisotropy changes significantly from the linear to the nonlinear regime of the MRI.
- Understanding the transition can shed light on the saturation of the instability.

Shell averages

- Shell averages have been used to predict/ determine power spectrum for MRI turbulence (Hawley et al 1995, Workman & Armitage 2008, Fromang 2010)

- => Shell averages might not describe anisotropic turbulence correctly

Stress tensor analysis

- Used to quantify anisotropy level, temporal variation and spatial distribution (Lumley 1977)

(a) Compute Reynolds and Maxwell stress

$$R_{ij} = \langle \delta v_i \, \delta v_j \rangle \,,$$
$$M_{ij} = \langle \delta B_i \, \delta B_j \rangle$$

(b) Normalize and subtract isotropic part

$$\mathcal{R}_{ij} = \frac{R_{ij}}{trace(R_{ij})} - \frac{1}{3}\delta_{ij}$$

(c) Calculate second and third invariants

$$\chi_2^{\mathcal{R}} = -(\lambda_1^2 + \lambda_2^2 + \lambda_3^2)$$
$$\chi_3^{\mathcal{R}} = \lambda_1 \, \lambda_2 \, \lambda_3$$

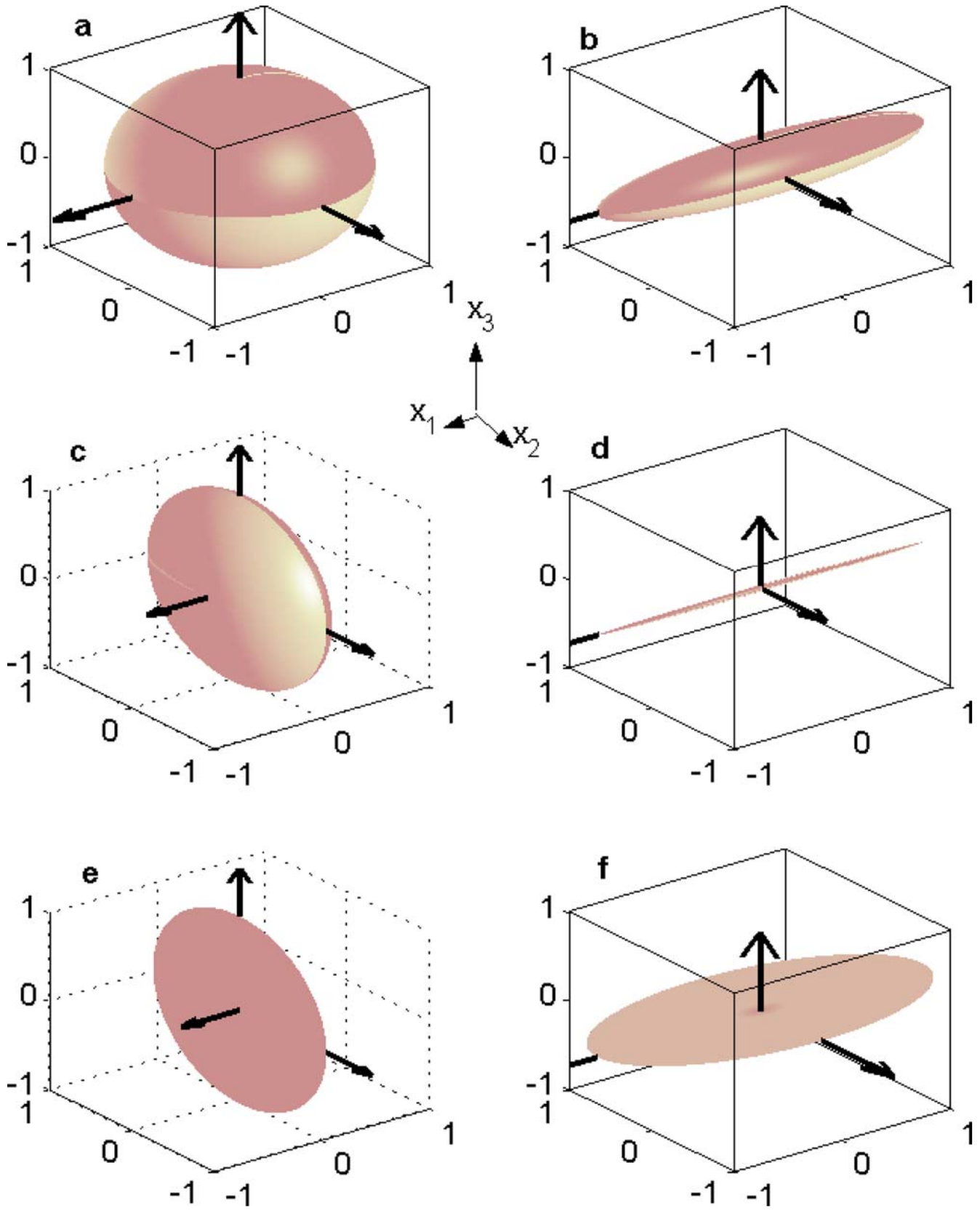

FIG. 3. Illustration of the ellipsoid shapes formed by the Reynolds stress tensor in different regions of the flow.

- Plot tensors as glyphs
- Axes are tensor eigenvalues
- Glyph points along principal eigenvector

Breakup of anisotropy

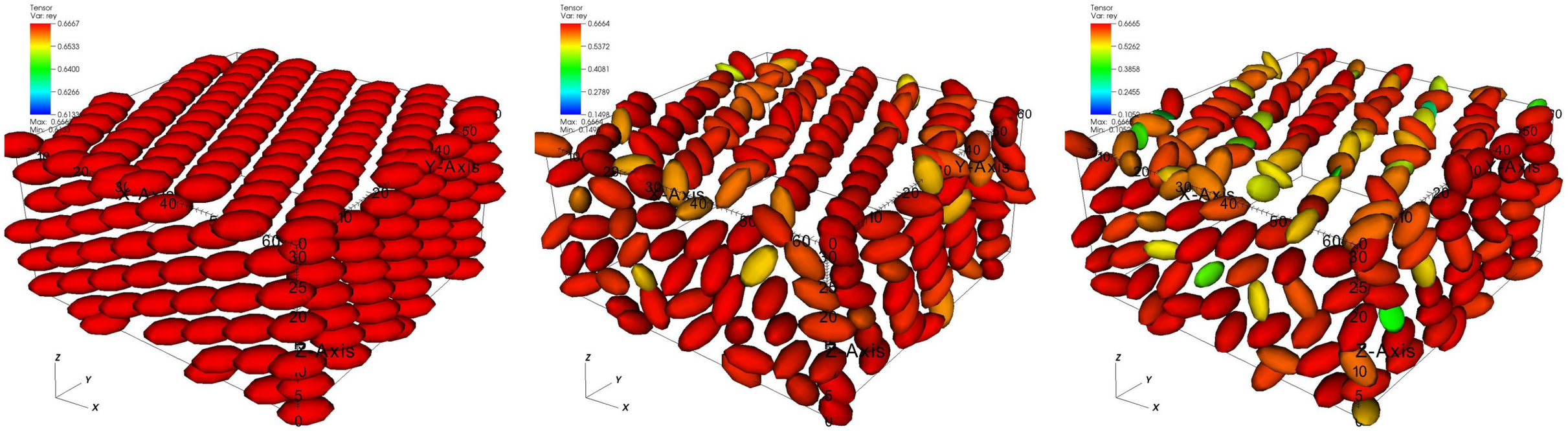

FIG. 7.— 3D tensor visualisation of the Reynolds stress anisotropy tensor, $\mathcal{R}$ at 6.2 orbits (immediately before saturation), 6.3 and 6.5 orbits. The ellipsoids are coloured with the magnitude of the maximum eigenvalue and axes of the ellipsoids are determined by the values of the three eigenvalues. The ellipsoids are aligned along the direction of the principal eigenvector. In the linear phase of the MRI growth, $\mathcal{R}$ is constant and aligned everywhere in the $x_{||}$ direction, which is the direction of principal stress for the MRI. The second panel shows $\mathcal{R}$ immediately after the onset of the parasitic modes, which appear as green and yellow ellipsoids. The parasites have grown and reduced the principal stress and scattered the direction of principal stress. The third panel shows $\mathcal{R}$ well into the saturated phase, with noticeable regions of peak stress, and regions where parasite modes are present.

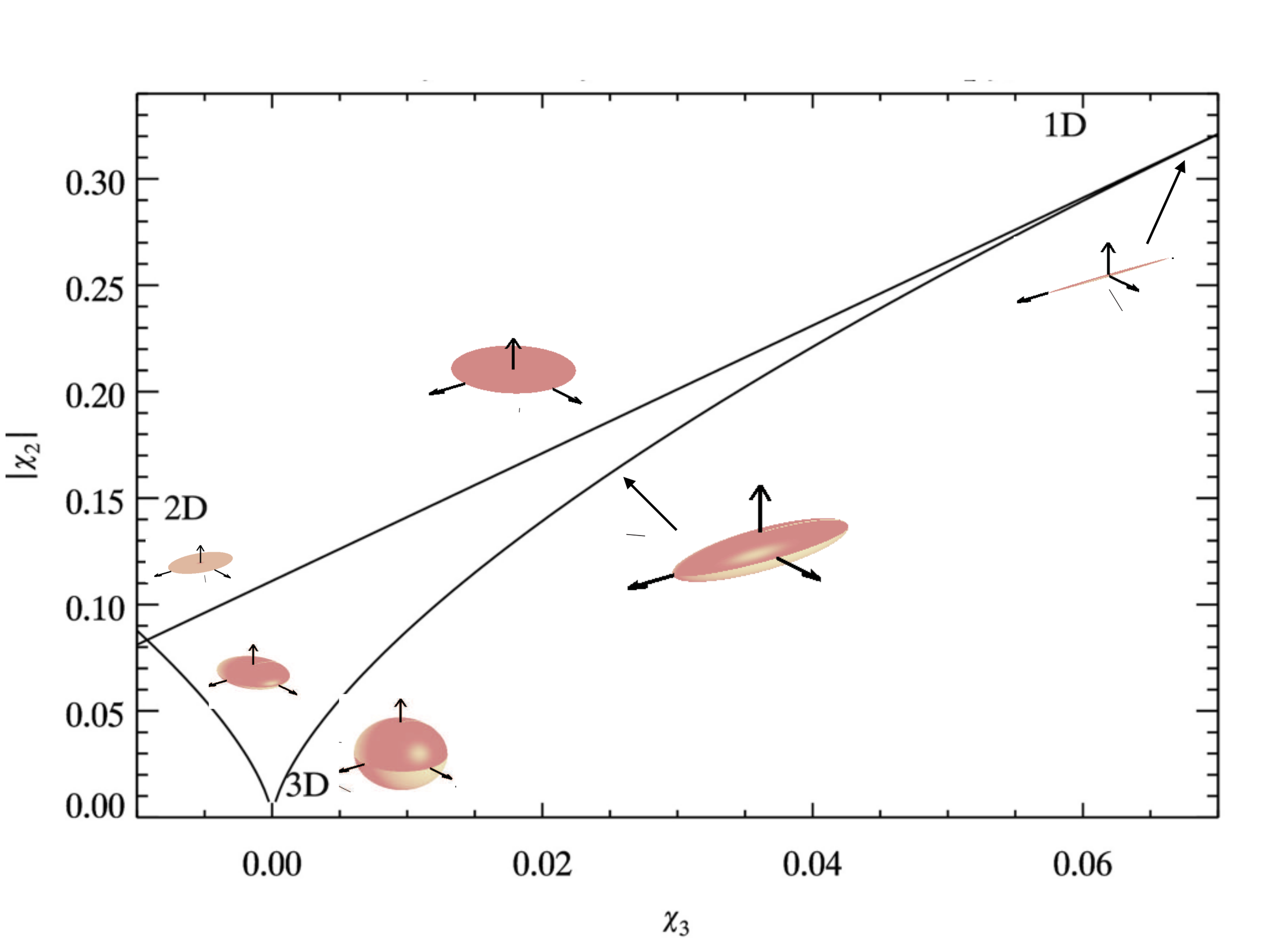
1D
2D
3D
0.30
0.25
0.20
0.15
0.10
0.05
0.00
$|\chi_2|$
0.00
0.02
0.04
0.06
χ_3

Temporal fluctuations in anisotropy

- Most of the power near the 1D vertex
- anisotropy shifts between 2D anisotropy locus and 3D anisotropy locus

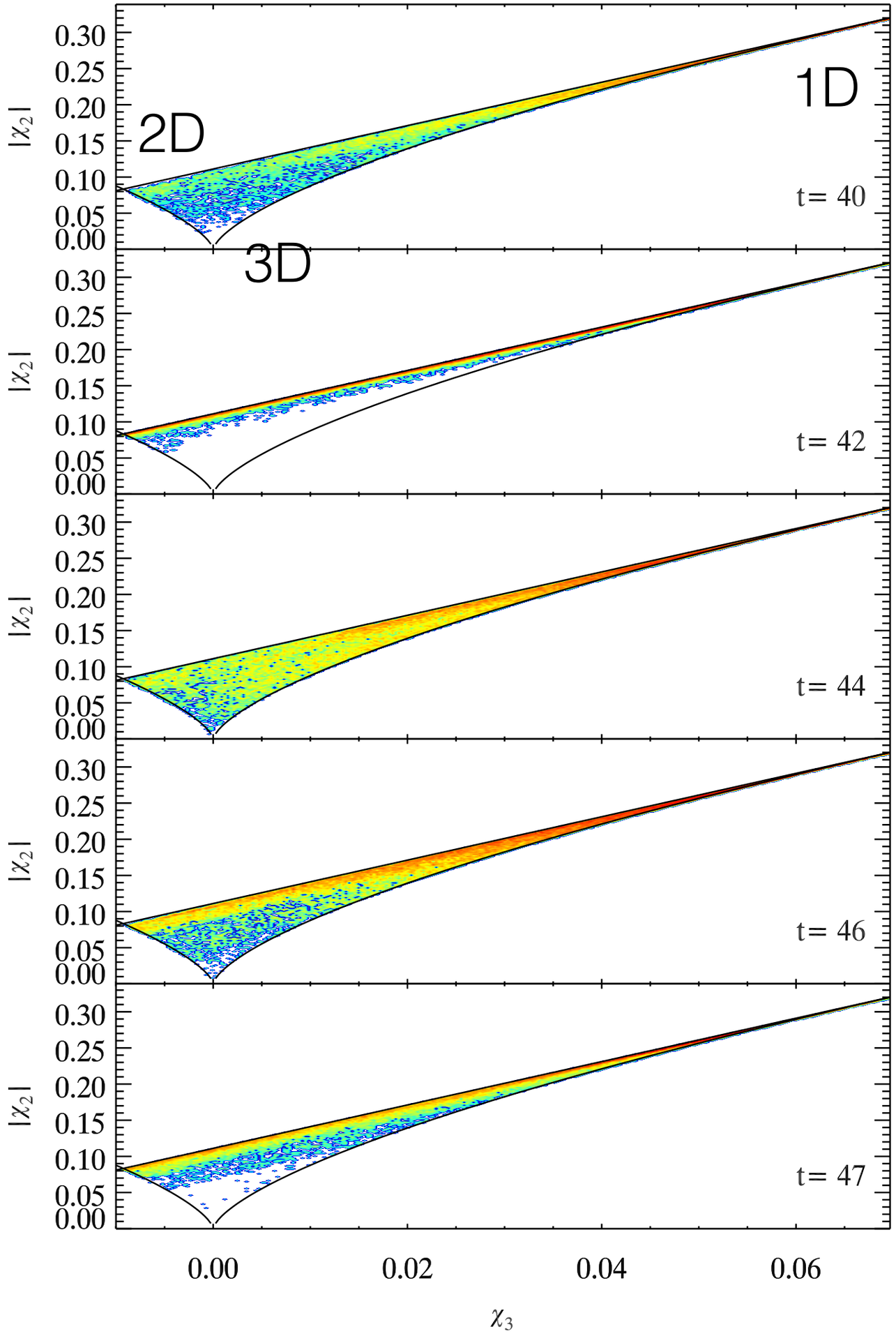

Spectral distribution of anisotropy

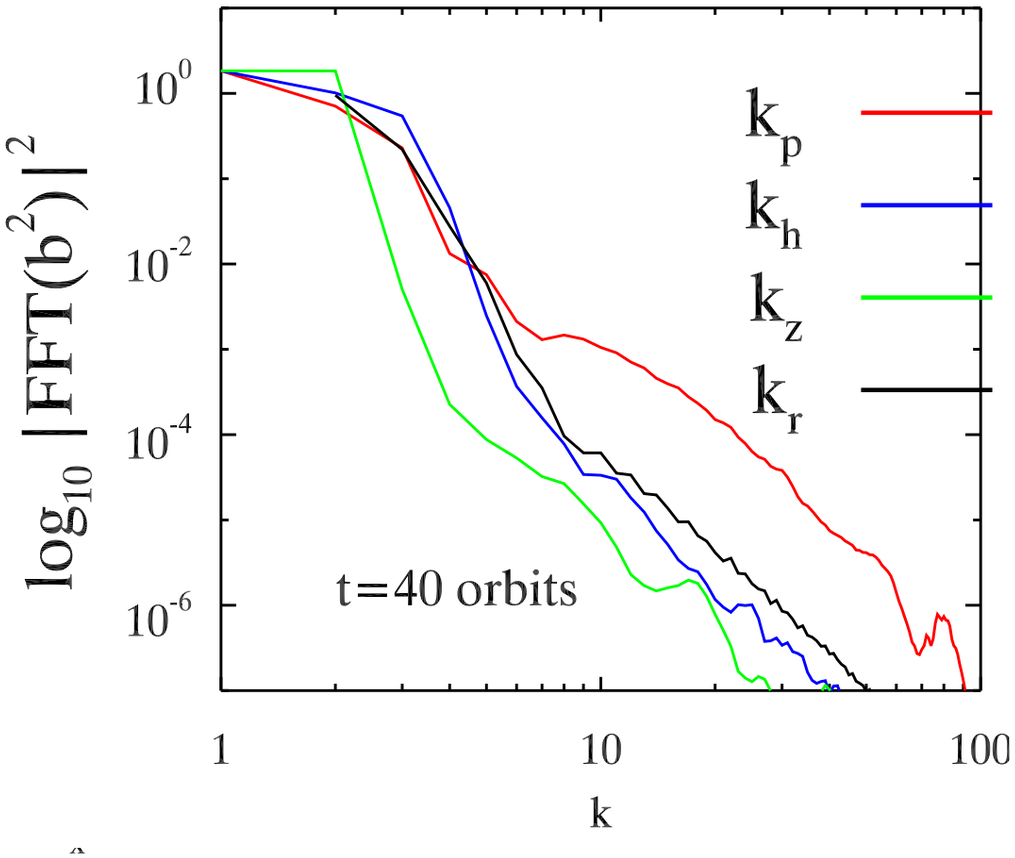

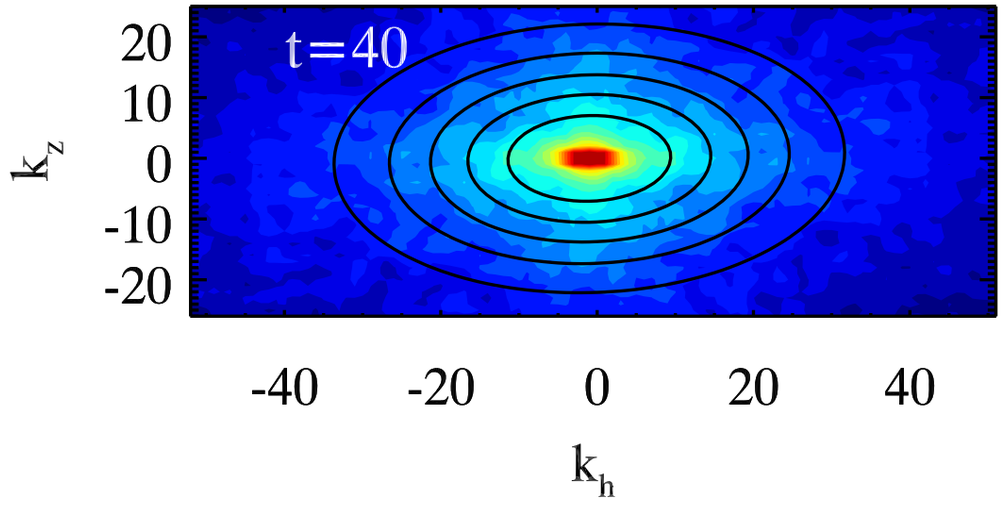

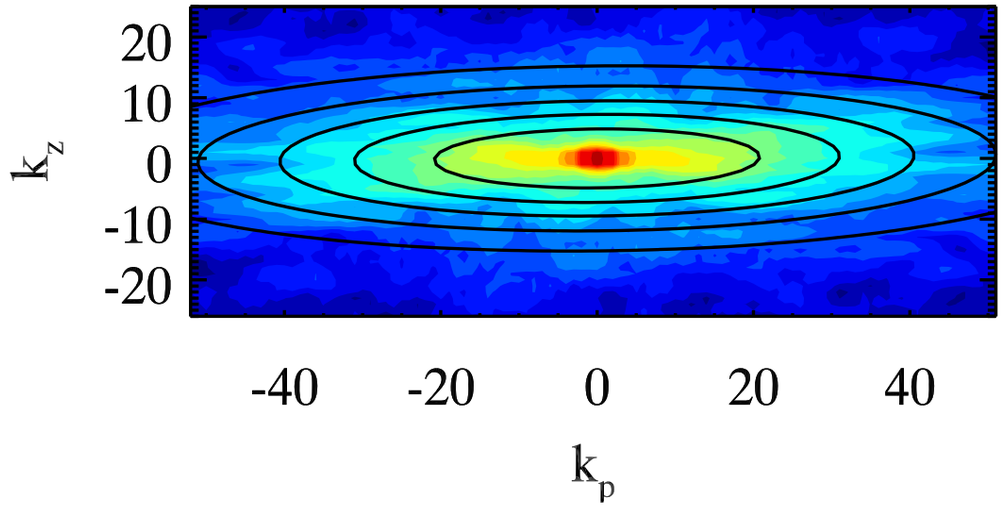

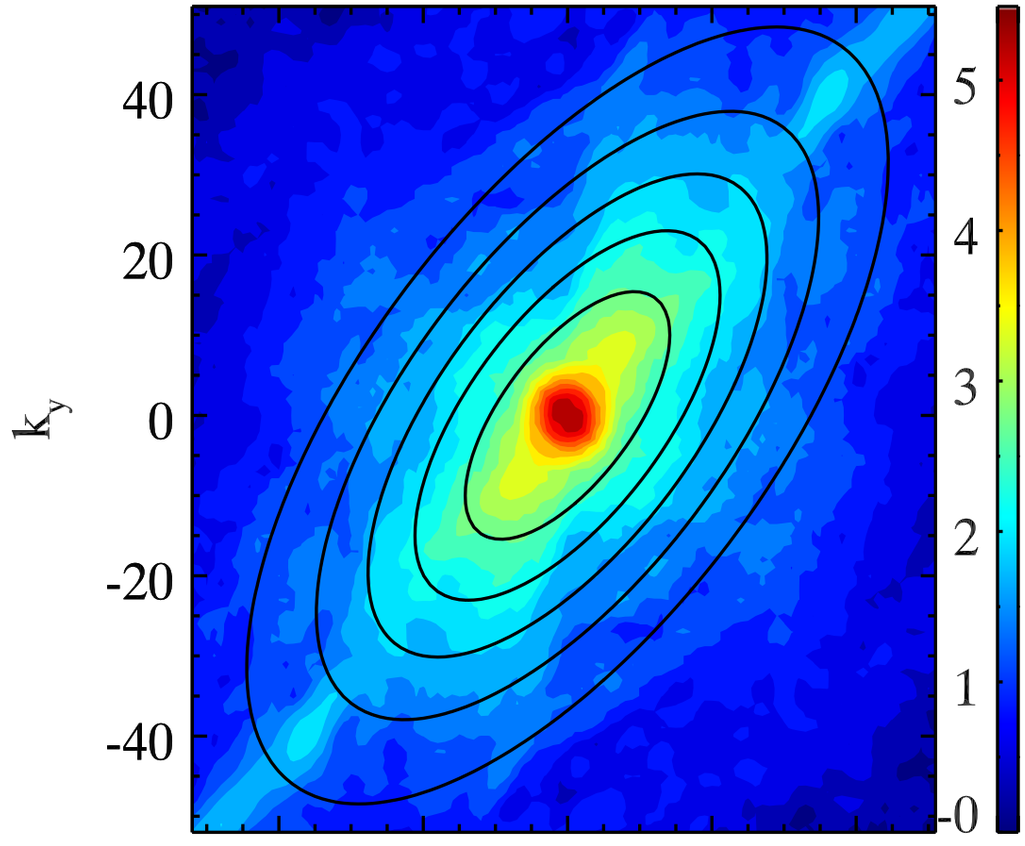

Perspectives

- Superexponential growth of parasite mode halts exponential growth of MRI mode

- Anisotropy of MRI turbulence varies with time

- Anisotropy of turbulence can influence morphology and longevity of flow structures, e.g. vortices

- Shell averages and simple isotropic scaling relations may not adequately describe properties of turbulence

- Using stress tensor invariants is a useful diagnostic of temporal variation of anisotropy, spatial and spectral distribution

Astron. Astrophys. 297, 273–284 (1995)

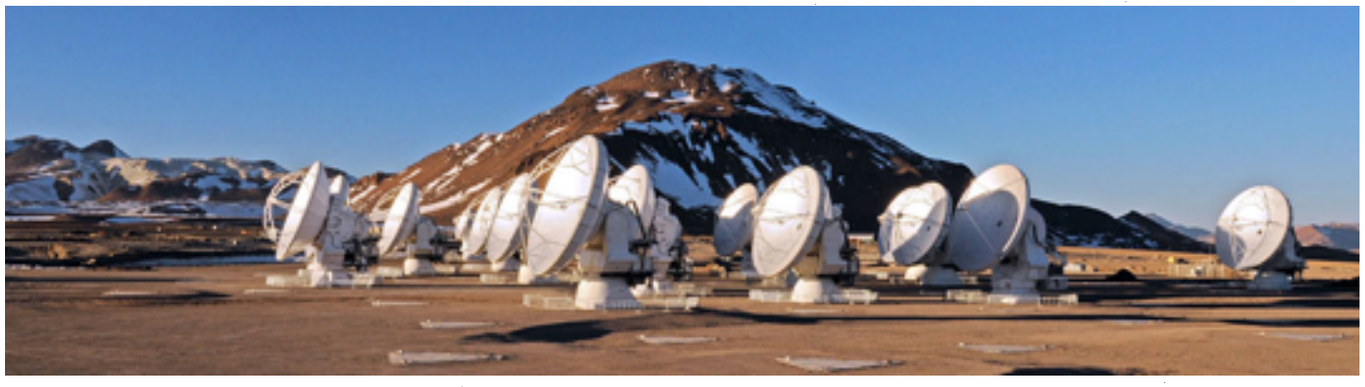

ASTRONOMY
AND
ASTROPHYSICS

Emission line signatures of anisotropic turbulence in accretion disks

Keith Horne[1,2]

[1] University of Utrecht, Astronomical Institute, Postbus 80000, NL-3508 TA Utrecht, The Netherlands
[2] Space Telescope Science Institute, 3700 San Martin Drive, Baltimore, MD 21218, USA

Received 8 March 1994 / Accepted 17 May 1994

Abstract. We investigate observable effects of anisotropic turbulence on the velocity profiles and eclipse behavior of emission lines from accretion disks. Turbulence expands the local line broadening profile, enhancing the surface brightness of saturated emission lines. Anisotropic turbulence produces anisotropic emission in such lines. The effects become observable when the turbulence exceeds the thermal velocity. Each term in the velocity-velocity correlation matrix produces a distinctive azimuthal pattern of enhanced emission-line surface brightness on the face of the accretion disk. These patterns express themselves as changes in the observable shapes of the double-peaked velocity profiles and eclipse behavior of the disk's emission lines. The best place to look for turbulence effects is in saturated emission lines of heavy elements such as Ca, Mg, and Fe, which have a smaller thermal velocity at a given sound speed, and at moderate inclination (60-70 degrees), since

the Rayleigh criterion. Nevertheless, turbulence and magnetic fields may be generated by the Balbus–Hawley instability (Balbus & Hawley 1991), which taps the Keplerian shear flow to amplify initially weak magnetic fields and generate turbulence on a dynamical timescale. This may lead to time-dependent dynamo action (Tout & Pringle 1992). Simulations of magnetohydrodynamic flow in shearing boxes (Hawley & Balbus 1991, 1992) suggest that the non-linear development of the instability is a vigorous anisotropic turbulent and magnetic flow that necessarily transports angular momentum outward, thus contributing to or even acounting for the anomalous viscosity (Balbus et al. 1995). As computer speeds increase, more realistic 3-D MHD simulations with gravity and radiation transport may soon yield predictions for the strength and character of the anisotropy in the fully-developed MHD turbulence of disks.